

Timescale Coalescence Makes Hidden Persistent Forcing Spectrally Dark

Yuda Bi,^{1,*} Chenyu Zhang,² and Vince D. Calhoun^{1,3}

¹*Translational Research in Neuroimaging and Data Science (TReNDS),
Georgia State University, Atlanta, Georgia 30303, USA*

²*School of Medical Technology, Beijing Institute of Technology, Beijing 100081, China*

³*School of Electrical and Computer Engineering,
Georgia Institute of Technology, Atlanta, Georgia 30332, USA*

(Dated: March 24, 2026)

Under coarse observation, detectability of unresolved slow forcing can be projection-controlled: only the component of the hidden-induced deformation normal to a reduced null manifold remains locally visible. We establish this exactly in a solvable driven AR(1)-by-AR(1) benchmark. The local Whittle/Kullback–Leibler distance from the true spectrum to the best nearby one-pole surrogate obeys $D_{\text{KL,loc}}^{\text{min}}(\lambda) = C\lambda^4 + O(\lambda^6)$, even though the observed spectrum itself is perturbed at $O(\lambda^2)$; detectability is therefore quartic, not quadratic, in coupling. The coefficient C is obtained in closed form and vanishes as $(a - b)^2$ when the hidden and intrinsic timescales coalesce, identifying a spectrally *dark* regime in which the leading perturbation is tangent to the reduced manifold. This yields a population boundary $\lambda_c^{\text{pop}}(N) \propto (\log N/N)^{1/4}$, with Whittle-BIC crossover near that scale. The benchmark exposes a broader geometric principle in reduced inference: tangent hidden effects are absorbed by reparametrization, whereas only surviving normal components control local distinguishability.

INTRODUCTION

Reduced inference under partial observation asks which hidden effects remain statistically visible after coarse graining. An unresolved slow mode may be dynamically active, inject low-frequency power, and yet still look indistinguishable from intrinsic persistence once the data are compressed to a coarse observable [1–5]. The same ambiguity appears in nonequilibrium inference under partial observation, where hidden slow variables can mask dissipation or irreversibility [6–9]. This is not just an interpretive nuisance: it changes whether an apparently persistent reduced mode should be read as intrinsic memory or as a surrogate for unresolved forcing [10, 11].

The issue is especially sharp in the frequency domain, because excess low-frequency power is already a reduced statistic rather than a direct fingerprint of mechanism [12, 13]. In reduced spectral inference one does not compare data to a full hidden-variable truth model. One refits the observed spectrum to the best nearby reduced surrogate, often a one-pole description, using Whittle likelihood or related criteria [14–19]. The central question is therefore geometric: not whether hidden forcing perturbs the spectrum at all, but whether that perturbation survives projection orthogonally to the best nearby reduced null.

This is a concrete instance of model-manifold compression under coarse graining: perturbation directions tangent to the reduced family are locally absorbed by reparametrization, whereas only the normal component remains asymptotically visible [5, 10, 11, 20]. A hidden driver can therefore generate a genuine $O(\lambda^2)$ spectral deformation while leaving no $O(\lambda^2)$ distinguishability after projection. In that sense, the hidden signa-

ture can be dynamically present yet *spectrally dark*. The same tangent-absorption geometry is suggested by driven Ornstein–Uhlenbeck precursors at timescale matching, but the discrete-time setting used here is the simplest one in which the projection algebra closes exactly on a compact frequency domain.

What has been missing is a minimal solvable setting in which this projection-controlled loss of visibility can be worked out exactly. Existing latent-variable and partially observed inference frameworks can detect hidden structure numerically or asymptotically in specific settings [21–23], but they do not isolate in closed form when a hidden slow perturbation is absorbed by motion along the reduced model manifold, nor whether detectability must begin at the same order as the raw spectral deformation itself.

We therefore define a precise notion of *spectrally dark*: at leading order, the driver contribution aligns with one-pole tangent directions and is absorbed before model-order penalties register it. In this stationary Gaussian AR(1) benchmark with nearby one-pole reduction, the issue is therefore a local projection question, not a generic hidden-detection theorem.

Here we provide that benchmark in the minimal analytically tractable driven AR(1)-by-AR(1) setting, where projection-controlled detectability can be worked out exactly. We prove a local theorem in the one-pole projection class: the Whittle/Kullback–Leibler divergence from the true spectrum to the best nearby one-pole surrogate satisfies $D_{\text{loc}}(\lambda) = C\lambda^4 + O(\lambda^6)$, even though hidden forcing perturbs the observed spectrum at $O(\lambda^2)$. The exact coefficient C vanishes as $(a - b)^2$ when the hidden and intrinsic timescales coalesce, yielding a leading population boundary of order $(\log N/N)^{1/4}$. The result therefore ex-

poses both the mechanism of delayed visibility and the scale at which that delay becomes operational; the coalescence signature enters explicitly through the closed-form prefactor. This is an exact benchmark for a broader organizing principle in reduced inference, not a universal theorem for arbitrary latent-variable models. Figures 1–3 show the mechanism, the exact quartic law, and the associated operational crossover.

SOLVABLE MODEL AND GEOMETRIC MECHANISM

We study the discrete-time benchmark

$$X_{t+1} = aX_t + \lambda F_t + \epsilon_t, \quad F_{t+1} = bF_t + \eta_t, \quad (1)$$

with $|a| < 1$, $|b| < 1$, $\epsilon_t \sim N(0, \sigma_\epsilon^2)$, $\eta_t \sim N(0, \sigma_\eta^2)$, and $\epsilon \perp \eta$. Only X_t is observed. The null family is the one-pole spectrum

$$S_{\text{null}}(\omega; \tilde{a}, \tilde{\sigma}^2) = \frac{\tilde{\sigma}^2}{P_{\tilde{a}}(\omega)}, \quad P_c(\omega) = 1 - 2c \cos \omega + c^2, \quad (2)$$

whereas the exact observed spectrum is

$$S_{\text{true}}(\omega; \lambda) = \frac{\sigma_\epsilon^2}{P_a(\omega)} + \frac{\lambda^2 \sigma_\eta^2}{P_a(\omega)P_b(\omega)} = S_0(\omega)(1 + \lambda^2 h(\omega)), \quad (3)$$

with $S_0(\omega) = \sigma_\epsilon^2/P_a(\omega)$ and $h(\omega) = \sigma_\eta^2/[\sigma_\epsilon^2 P_b(\omega)]$. The hidden driver therefore enters as an $O(\lambda^2)$ perturbation of the null spectrum. In numerical work we subtract the mean and drop the DC bin; the technical rationale is given in the Supplemental Material.

The key distinction is already visible here. Equation (3) shows that hidden forcing deforms the observed spectrum at $O(\lambda^2)$, but reduced inference does not test this raw deformation against a fixed null point. It reoptimizes within the null family. Detectability is therefore governed not by the existence of excess low-frequency structure alone, but by the part of that structure that cannot be re-expressed by a nearby one-pole surrogate.

For the theorem statement we work in the local stationary AR(1) regime with $|a| < 1$, $|b| < 1$, and finite-variance independent innovations. In this setting, the local Whittle objective is the standard tractable surrogate for the KL geometry in frequency space and provides the shared objective across the mechanistic derivation and the finite-sample model-selection experiments. Using AIC/BIC language is therefore a corollary rather than a separate calibration: the objective defines the local contrast, while the model-count gap sets the operational boundary scale used below.

To turn Eq. (3) into a detectability statement, one must compare the true spectrum not to the null point itself but to the best nearby one-pole fit. Write

$$\tilde{a} = a + \delta a, \quad \tilde{\sigma}^2 = \sigma_\epsilon^2 + \delta \sigma^2. \quad (4)$$

Then the relative null spectrum expands as

$$\frac{S_{\text{null}}(\omega; \tilde{a}, \tilde{\sigma}^2)}{S_0(\omega)} = 1 + u\tilde{e}_1(\omega) + v\tilde{e}_2(\omega) + O(u^2 + v^2 + uv), \quad (5)$$

where

$$u = \frac{\delta \sigma^2}{\sigma_\epsilon^2}, \quad v = \delta a, \quad (6)$$

$$\tilde{e}_1(\omega) = 1, \quad \tilde{e}_2(\omega) = \frac{2(\cos \omega - a)}{P_a(\omega)}.$$

The one-pole manifold therefore has a two-dimensional tangent space $\mathcal{T} = \text{span}\{\tilde{e}_1, \tilde{e}_2\}$ at the null point. In these coordinates the relevant population divergence is

$$D_{\text{KL}}(S_1 \| S_2) = \frac{1}{4\pi} \int_{-\pi}^{\pi} \left[\frac{S_1(\omega)}{S_2(\omega)} - \log \frac{S_1(\omega)}{S_2(\omega)} - 1 \right] d\omega. \quad (7)$$

with $\langle f, g \rangle_{L^2} := \frac{1}{2\pi} \int_{-\pi}^{\pi} f(\omega)g(\omega) d\omega$. Using the local scalar expansion $(1 + \delta) - \log(1 + \delta) - 1 = \delta^2/2 + O(\delta^3)$, the fitting problem reduces to

$$D_{\text{KL}}(S_{\text{true}}(\cdot; \lambda) \| S_{\text{null}}(\cdot; \tilde{a}, \tilde{\sigma}^2)) = \frac{1}{4} \left\| \lambda^2 h - u\tilde{e}_1 - v\tilde{e}_2 \right\|_{L^2}^2 + O((|u| + |v| + \lambda^2)^3). \quad (8)$$

Equation (8) is the local geometry in one line: the best one-pole fit is the orthogonal projection of the leading perturbation onto the tangent space of the null manifold. It is useful to separate the three objects that now appear. The function h is the physical $O(\lambda^2)$ deformation induced by the hidden driver; $\Pi_{\mathcal{T}}h$ determines how the pseudo-true null model drifts along the reduced manifold; and $(I - \Pi_{\mathcal{T}})h$ is the only part that can accumulate leading-order evidence against the null. The theorem is therefore an order statement about the normal geometry of the reduced family, not just a coefficient expansion for a particular AR benchmark. The same projection data also determine how the best one-pole surrogate moves along that manifold:

$$\tilde{\sigma}^{2*}(\lambda) = \sigma_\epsilon^2 + \lambda^2 \frac{\sigma_\eta^2}{1 - b^2} + O(\lambda^4),$$

$$\tilde{a}^*(\lambda) = a + \lambda^2 \frac{\sigma_\eta^2}{\sigma_\epsilon^2} \frac{b(1 - a^2)}{(1 - ab)(1 - b^2)} + O(\lambda^4).$$

These pseudo-true shifts make tangent absorption concrete: the best one-pole fit drifts along the null manifold exactly in the direction predicted by the projection picture.

Figure 1 shows why this is not yet the detectability law. Away from timescale matching, the best one-pole fit leaves a visible residual spectral shape. At pole coalescence, by contrast, the residual is strongly suppressed because the leading perturbation becomes tangent to the one-pole manifold and is reabsorbed by the best null reparametrization.

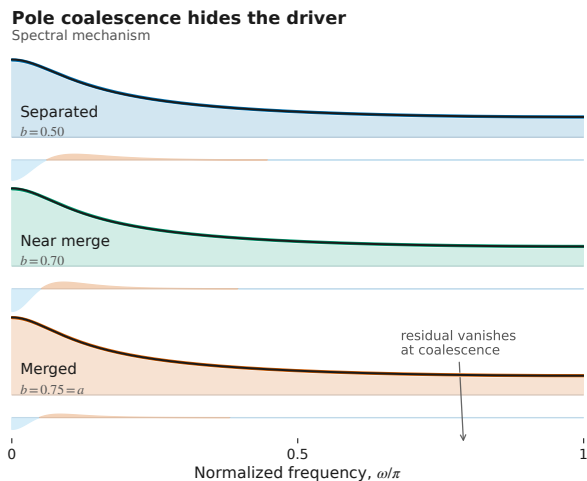


FIG. 1. Pole coalescence hides the driver. For this mechanism panel, $a = 0.75$, $\lambda = 0.12$, and $\sigma_\epsilon^2 = \sigma_\eta^2 = 1$, while the hidden persistence is $b = 0.50, 0.70$, and $0.75 = a$ from top to bottom. The exact driven spectrum is compared with the best-fit one-pole null spectrum for separated, near-coalescent, and merged timescales; the merged case corresponds to exact coalescence, $b = a$. The residual spectral shape is pronounced away from coalescence and is strongly suppressed as the hidden and intrinsic poles merge.

QUARTIC DETECTABILITY LAW

The tangent basis in Eq. (6) is orthogonal in the normalized L^2 inner product,

$$\langle \tilde{e}_1, \tilde{e}_2 \rangle = 0, \quad \|\tilde{e}_1\|^2 = 1, \quad \|\tilde{e}_2\|^2 = \frac{2}{1-a^2}, \quad (9)$$

so the local Hessian of the Whittle objective is positive definite. Writing

$$R = h - \Pi_\tau h \quad (10)$$

for the normal residual after tangent absorption, the nearby pseudo-true one-pole branch satisfies

$$\begin{aligned} D_{\text{KL,loc}}^{\min}(\lambda) &= D_{\text{KL}}(S_{\text{true}}(\cdot; \lambda) \| S_{\text{null}}(\cdot; \tilde{a}, \tilde{\sigma}^2)) \\ &\Big|_{(\tilde{a}, \tilde{\sigma}^2) = (\tilde{a}^*(\lambda), \tilde{\sigma}^{2*}(\lambda))} \\ &= \frac{\lambda^4}{4} \|R\|_{L^2}^2 + O(\lambda^6). \end{aligned} \quad (11)$$

Equation (11) is the geometric content of the theorem: after tangent absorption, the $O(\lambda^2)$ perturbation survives only through its normal component, so the detectability order is projection-controlled and begins at quartic order. Because the tangent basis is orthogonal and the local Hessian is positive definite, the reduced Whittle objective admits a unique nearby minimizer branch for sufficiently small $|\lambda|$. The theorem therefore controls a well-defined pseudo-true one-pole continuation of the

null model rather than an informal best-fit heuristic; the derivation of the tangent basis, projection coefficients, local minimizer, and DC-bin implementation is given in the Supplemental Material.

Theorem 1. For each fixed (a, b) with $|a| < 1$ and $|b| < 1$, there exists $\lambda_0(a, b) > 0$ such that for $|\lambda| < \lambda_0(a, b)$ the local Whittle minimizer branch within the one-pole projection class exists uniquely and the associated local minimum satisfies

$$D_{\text{KL,loc}}^{\min}(\lambda) = C(a, b, \sigma_\epsilon, \sigma_\eta) \lambda^4 + O(\lambda^6), \quad (12)$$

with $C \geq 0$ and

$$C = 0 \iff (a = b) \text{ or } (b = 0). \quad (13)$$

For the solvable model in Eq. (1), the projection integrals can be evaluated exactly in the Supplemental Material, so Eq. (11) closes as

$$D_{\text{KL,loc}}^{\min}(\lambda) = C(a, b, \sigma_\epsilon, \sigma_\eta) \lambda^4 + O(\lambda^6), \quad (14)$$

with

$$C(a, b, \sigma_\epsilon, \sigma_\eta) = \frac{\sigma_\eta^4}{2\sigma_\epsilon^4} \frac{b^2(a-b)^2}{(1-b^2)^3(1-ab)^2}. \quad (15)$$

Hence

$$C = 0 \iff (a = b) \text{ or } (b = 0). \quad (16)$$

For persistent hidden drivers ($b \neq 0$), the quartic coefficient is strictly positive away from coalescence and vanishes exactly on the timescale-matching line $a = b$. In the present solvable class,

$$C(a, b, \sigma_\epsilon, \sigma_\eta) \propto (a-b)^2 \quad \text{as } b \rightarrow a. \quad (17)$$

Equation (15) is the main theorem-level statement. Hidden forcing becomes hard to detect not because its amplitude disappears, but because tangent reparametrization absorbs the leading spectral deformation, leaving quartic onset as the first surviving normal order. The factor $(a-b)^2$ is the coalescence signature: when the hidden pole merges with the intrinsic one, the surviving normal coefficient vanishes and the quartic prefactor collapses. At exact coalescence, higher-order terms take over. The central point is therefore the gap between the $O(\lambda^2)$ dynamical perturbation and the $O(\lambda^4)$ distinguishability.

This is why the quartic law is more than a high-order asymptotic curiosity. It identifies which part of the hidden signal is statistically operative after coarse-grained refitting. The driver is already present in the $O(\lambda^2)$ spectral deformation and in the $O(\lambda^2)$ pseudo-true parameter shifts, but those contributions remain silent to leading order whenever they are tangent. Quartic onset is the first order at which a normal mismatch survives reparametrization and can register in the reduced objective.

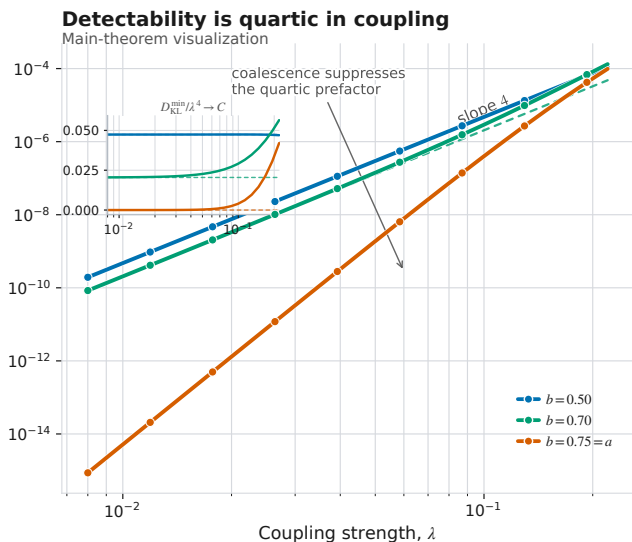


FIG. 2. Detectability is quartic in coupling. Exact numerical minimization of the one-pole projection problem for $a = 0.75$, $\sigma_\epsilon^2 = \sigma_\eta^2 = 1$, and $b = 0.50, 0.70, 0.75 = a$. Away from coalescence the quartic residual is visible; timescale matching suppresses it through a vanishing prefactor C (inset).

Figure 2 displays the theorem in population numerics. All noncoalesced cases exhibit quartic onset, while the entire curve is pushed downward as $a \rightarrow b$ because the quartic prefactor is suppressed. This is a local weak-coupling theorem for the nearby pseudo-true one-pole branch; exact global minimization below verifies that the tested parameter regimes remain on that branch.

Mechanistic lesson. The solvable benchmark suggests a broader local organizing principle. A good reduced one-pole fit need not exclude hidden slow forcing; it may indicate that the leading hidden perturbation lies largely in a tangent direction of the reduced manifold and is absorbed by reparametrization [5, 10, 20]. If a reduced spectral family forms a smooth manifold through S_0 , the true spectrum satisfies $S_{\text{true}}(\lambda) = S_0(1 + \lambda^2 h + O(\lambda^4))$, and the local Whittle Hessian is positive definite on the tangent space \mathcal{T} , then the same quadratic reduction formally yields

$$D_{\text{KL}}^{\text{min}}(\lambda) = \frac{\lambda^4}{4} \|(I - \Pi_{\mathcal{T}})h\|^2 + O(\lambda^6).$$

The present solvable benchmark is the exact one-pole realization of this candidate geometric principle, not a universal theorem for arbitrary model classes.

NUMERICAL AND OPERATIONAL TESTS

Equation (14) immediately yields a leading-order operational boundary for the data required to resolve hidden forcing. Define $\lambda_c^{\text{pop}}(N)$ by balancing the local asymp-

otic KL gain against the BIC penalty in the Whittle-BIC readout,

$$N D_{\text{KL},\text{loc}}^{\text{min}}(\lambda_c^{\text{pop}}) = \frac{\Delta k}{2} \log N. \quad (18)$$

For the effective two-pole alternative used in the Whittle-BIC tests, $\Delta k = 2$, so Eqs. (14) and (15) give

$$\lambda_c^{\text{pop}}(N) = \left[\frac{2\sigma_\epsilon^4(1-b^2)^3(1-ab)^2 \log N}{\sigma_\eta^4 b^2 (a-b)^2 N} \right]^{1/4} (1 + o(1)). \quad (19)$$

Thus

$$\lambda_c^{\text{pop}}(N) \propto (\log N/N)^{1/4}, \quad \lambda_c^{\text{pop}} \propto |a-b|^{-1/2}. \quad (20)$$

The first scaling is the sample-complexity imprint of projection-controlled detectability: hidden forcing becomes detectable only at quartic order in coupling. The second says that coalescence further suppresses visibility as $a \rightarrow b$. These equations define a leading-order population boundary, not an exact finite-sample 50%-power threshold. At fixed scaled coupling, Eq. (20) implies $N/\log N \propto |a-b|^{-2}$, so shrinking the pole separation from 0.10 to 0.02 raises the leading-order data requirement by about a factor of 25.

At finite N the boundary should be read as a turnover predictor: curvature, finite-frequency effects, and fitting tolerance shift the curves without changing the leading scaling. Exact global minimization over the full stationary one-pole family reproduces quartic onset, boundary scaling, and coalescence suppression, showing that the tested regimes remain on the same branch as the local theorem. Figure 3 then uses Whittle-BIC only as an operational readout of this geometry-controlled boundary: model comparison turns over near the scaled threshold predicted by Eq. (19). Additional finite-sample checks, regime-robustness stress tests, mild Student- t misspecification, and the enriched ARMA(1,1) null in the Supplemental Material support the same interpretation.

BEYOND THE STRICT ONE-POLE NULL

The mechanism is not tied to the strict AR(1) null. For the simplest one-pole enrichment, an ARMA(1,1) family with one pole and one zero still gives $D_{\text{KL},\text{loc},(1,1)}^{\text{min}}(\lambda) = C_{(1,1)}\lambda^4 + O(\lambda^6)$ with $C_{(1,1)} = b^2 C$. Enlarging the null therefore weakens but does not eliminate tangent absorption.

DISCUSSION

This Letter identifies a local organizing principle for reduced inference: the detectable component of hidden

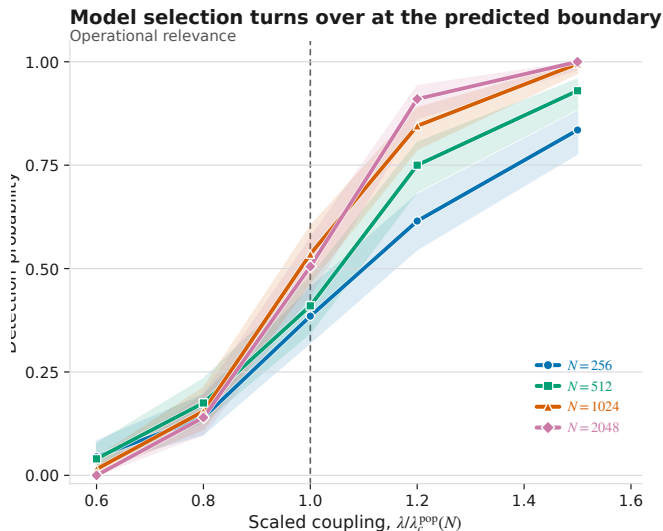


FIG. 3. Model selection turns over near the predicted scaled boundary. Whittle-BIC detection probability is plotted against $\lambda/\lambda_c^{\text{pop}}(N)$ for the baseline parameters $(a, b, \sigma_e^2, \sigma_\eta^2) = (0.95, 0.8, 1, 1)$ and $N = 256\text{--}2048$ (200 repetitions per point). The common crossover near unity is consistent with the asymptotic boundary but not with exact finite-size collapse.

forcing is the part of its deformation that survives orthogonally to the reduced null manifold. Equivalently, detectability is controlled by

$$D_{\text{loc}}(\lambda) = C\lambda^4 + O(\lambda^6),$$

not by the raw $O(\lambda^2)$ spectral deformation. The prefactor $C \propto (a - b)^2$ converts this geometry into a concrete prediction, a closed boundary

$$\lambda_c^{\text{pop}}(N) \sim (\log N/N)^{1/4},$$

with explicit constants.

The driven AR(1)-by-AR(1) model is the minimal solvable setting in which this mechanism can be worked out exactly. In that benchmark, tangent absorption selects quartic onset, timescale coalescence suppresses the surviving normal coefficient as $(a - b)^2$, and the same geometry reshapes the leading sample-complexity scale. The finite-sample suite then shows the corresponding delayed turnover near the predicted scaled boundary.

The scope is intentionally local: stationary Gaussian AR(1) latents, weak coupling around $\lambda = 0$, and one-pole (or one-pole ARMA(1,1)) reduced classes. We do not claim a universal latent-detection theorem for arbitrary hidden-variable models. The point is narrower and cleaner: in a minimal exact benchmark, reduced-inference geometry alone can demote detectability order, suppress visibility at coalescence, and set the leading operational scale.

* ybi3@student.gsu.edu

- [1] K. Hasselmann, Stochastic climate models: Part I. theory, *Tellus A: Dynamic Meteorology and Oceanography* **28**, 473 (1976).
- [2] C. Frankignoul and K. Hasselmann, Stochastic climate models, part II application to sea-surface temperature anomalies and thermocline variability, *Tellus A: Dynamic Meteorology and Oceanography* **29**, 289 (1977).
- [3] C. Penland and P. D. Sardeshmukh, The optimal growth of tropical sea surface temperature anomalies, *Journal of Climate* **8**, 1999 (1995).
- [4] A. J. Majda, I. Timofeyev, and E. Vanden-Eijnden, Models for stochastic climate prediction, *Proceedings of the National Academy of Sciences of the United States of America* **96**, 14687 (1999).
- [5] A. J. Chorin, O. H. Hald, and R. Kupferman, Optimal prediction and the Mori-Zwanzig representation of irreversible processes, *Proceedings of the National Academy of Sciences of the United States of America* **97**, 2968 (2000).
- [6] É. Roldán and J. M. R. Parrondo, Estimating dissipation from single stationary trajectories, *Physical Review Letters* **105**, 150607 (2010).
- [7] J. Mehl, B. Lander, C. Bechinger, V. Blickle, and U. Seifert, Role of hidden slow degrees of freedom in the fluctuation theorem, *Physical Review Letters* **108**, 220601 (2012).
- [8] D. J. Skinner and J. Dunkel, Estimating entropy production from waiting time distributions, *Physical Review Letters* **127**, 198101 (2021).
- [9] U. Seifert, From stochastic thermodynamics to thermodynamic inference, *Annual Review of Condensed Matter Physics* **10**, 171 (2019).
- [10] N. Israeli and N. Goldenfeld, Coarse-graining of cellular automata, emergence, and the predictability of complex systems, *Physical Review E* **73**, 026203 (2006).
- [11] B. B. Machta, R. Chachra, M. K. Transtrum, and J. P. Sethna, Parameter space compression underlies emergent theories and predictive models, *Science* **342**, 604 (2013).
- [12] M. B. Priestley, *Spectral Analysis and Time Series* (Academic Press, London, 1981).
- [13] M. Ghil, M. R. Allen, M. D. Dettinger, K. Ide, D. Kondrashov, M. E. Mann, A. W. Robertson, A. Saunders, Y. Tian, F. Varadi, and P. Yiou, Advanced spectral methods for climatic time series, *Reviews of Geophysics* **40**, 1003 (2002).
- [14] P. Whittle, The analysis of multiple stationary time series, *Journal of the Royal Statistical Society: Series B* **15**, 125 (1953).
- [15] K. Dzhaparidze, *Parameter Estimation and Hypothesis Testing in Spectral Analysis of Stationary Time Series* (Springer, New York, 1986).
- [16] M. Taniguchi and Y. Kakizawa, *Asymptotic Theory of Statistical Inference for Time Series* (Springer, New York, 2000).
- [17] H. Akaike, A new look at the statistical model identification, *IEEE Transactions on Automatic Control* **19**, 716 (1974).
- [18] G. Schwarz, Estimating the dimension of a model, *The Annals of Statistics* **6**, 461 (1978).
- [19] E. J. Hannan and J. Rissanen, Recursive estimation of

- mixed autoregressive-moving average order, *Biometrika* **69**, 81 (1982).
- [20] D. Givon, R. Kupferman, and A. Stuart, Extracting macroscopic dynamics: Model problems and algorithms, *Nonlinearity* **17**, R55 (2004).
- [21] L. R. Rabiner, A tutorial on hidden markov models and selected applications in speech recognition, *Proceedings of the IEEE* **77**, 257 (1989).
- [22] Y. Ephraim and N. Merhav, Hidden markov processes, *IEEE Transactions on Information Theory* **48**, 1518 (2002).
- [23] E. S. Allman, C. Matias, and J. A. Rhodes, Identifiability of parameters in latent structure models with many observed variables, *The Annals of Statistics* **37**, 3099 (2009).
- [24] R. Kawai, J. M. R. Parrondo, and C. Van den Broeck, Dissipation: The phase-space perspective, *Physical Review Letters* **98**, 080602 (2007).
- [25] M. Esposito and C. Van den Broeck, Three faces of the second law. i. master equation formulation, *Physical Review E* **82**, 011143 (2010).
- [26] D. Hartich, A. C. Barato, and U. Seifert, Stochastic thermodynamics of bipartite systems: Transfer entropy inequalities and a maxwell's demon interpretation, *Journal of Statistical Mechanics: Theory and Experiment* **2014**, P02016 (2014).
- [27] A. C. Barato and U. Seifert, Thermodynamic uncertainty relation for biomolecular processes, *Physical Review Letters* **114**, 158101 (2015).
- [28] G. R. North, R. F. Cahalan, and J. A. Coakley, Energy balance climate models, *Reviews of Geophysics and Space Physics* **19**, 91 (1981).
- [29] G. E. Crooks, Entropy production fluctuation theorem and the nonequilibrium work relation for free energy differences, *Physical Review E* **60**, 2721 (1999).
- [30] C. Jarzynski, Nonequilibrium equality for free energy differences, *Physical Review Letters* **78**, 2690 (1997).
- [31] U. Seifert, Stochastic thermodynamics, fluctuation theorems and molecular machines, *Reports on Progress in Physics* **75**, 126001 (2012).
- [32] C. Jarzynski, Equalities and inequalities: Irreversibility and the second law of thermodynamics at the nanoscale, *Annual Review of Condensed Matter Physics* **2**, 329 (2011).
- [33] J. M. R. Parrondo, J. M. Horowitz, and T. Sagawa, Thermodynamics of information, *Nature Physics* **11**, 131 (2015).
- [34] J. M. Horowitz and M. Esposito, Thermodynamics with continuous information flow, *Physical Review X* **4**, 031015 (2014).
- [35] N. Shiraishi and T. Sagawa, Fluctuation theorem for partially masked nonequilibrium dynamics, *Physical Review E* **91**, 012130 (2015).
- [36] M. Polettni and M. Esposito, Effective thermodynamics for a marginal observer, *Physical Review Letters* **119**, 240601 (2017).
- [37] G. Bisker, M. Polettni, T. R. Gingrich, J. M. Horowitz, and J. M. R. Parrondo, Hierarchical bounds on entropy production inferred from partial information, *Journal of Statistical Mechanics: Theory and Experiment* **2017**, 093210 (2017).
- [38] J. Schnakenberg, Network theory of microscopic and macroscopic behavior of master equation systems, *Reviews of Modern Physics* **48**, 571 (1976).
- [39] P. J. Brockwell and R. A. Davis, *Introduction to Time Series and Forecasting*, 3rd ed. (Springer, Cham, 2016).
- [40] R. H. Shumway and D. S. Stoffer, *Time Series Analysis and Its Applications: With R Examples*, 4th ed. (Springer, Cham, 2017).
- [41] K. P. Burnham and D. R. Anderson, *Model Selection and Multimodel Inference: A Practical Information-Theoretic Approach*, 2nd ed. (Springer, New York, 2002).
- [42] G. Claeskens and N. L. Hjort, *Model Selection and Model Averaging* (Cambridge University Press, Cambridge, 2008).
- [43] P. Stoica and Y. Selen, Model-order selection: A review of information criterion rules, *IEEE Signal Processing Magazine* **21**, 36 (2004).
- [44] C. M. Hurvich and C.-L. Tsai, Regression and time series model selection in small samples, *Biometrika* **76**, 297 (1989).
- [45] C. W. J. Granger, Investigating causal relations by econometric models and cross-spectral methods, *Econometrica* **37**, 424 (1969).
- [46] C. A. Sims, Money, income, and causality, *The American Economic Review* **62**, 540 (1972).
- [47] J. Geweke, Measurement of linear dependence and feedback between multiple time series, *Journal of the American Statistical Association* **77**, 304 (1982).
- [48] B. G. Leroux, Maximum-likelihood estimation for hidden Markov models, *Stochastic Processes and their Applications* **40**, 127 (1992).
- [49] O. Cappé, E. Moulines, and T. Rydén, *Inference in Hidden Markov Models* (Springer, New York, 2005).
- [50] D. Hsu, S. M. Kakade, and T. Zhang, A spectral algorithm for learning hidden markov models, *Journal of Computer and System Sciences* **78**, 1460 (2012).
- [51] G. Verbeke and G. Molenberghs, Modeling through latent variables, *Annual Review of Statistics and Its Application* **4**, 267 (2017).

Supplemental Material

Timescale Coalescence Makes Hidden Persistent Forcing Spectrally Dark

Appendices A–K provide derivations and validations supporting the main text, from geometry and proofs to exact numerics, operational stress tests, and scope discussion.

Appendix A: Supplementary Overview and Literature Positioning

These appendices record the derivations supporting the main-text theorem and its numerical checks. The physical question is whether an observed slow mode is intrinsically persistent or only appears persistent because it is driven by an unresolved persistent force. That ambiguity is central to stochastic climate modeling [1–3], reduced nonequilibrium inference with hidden slow variables [6–9], and thermodynamic inference under coarse observation [24–27].

Energy-balance climate models, stochastic mode-reduction schemes, and advanced spectral analyses reinforce the same point from complementary directions [4, 13, 28]. In nonequilibrium settings, fluctuation theorems, thermodynamics of information, and marginal-observer constructions provide parallel motivation for asking what reduced observations can still distinguish [29–38].

The technical setting is the intersection of Whittle spectral inference [14, 16], classical spectral-analysis practice [12, 39, 40], information-criterion model selection [15, 17–19, 41–44], hidden-cause inference in time series [45–47], and latent-state recovery [21–23, 48–51]. What is specific to the present work is the exact quartic detectability law and the explicit coalescence mechanism within the one-pole projection class.

What is proved exactly in the appendices below is:

- a local quartic detectability law in the one-pole projection class;
- a closed form for the quartic coefficient;
- a quantitative coalescence law $C \propto (a - b)^2$;
- an enriched-null ARMA(1, 1) corollary that makes model-class dependence explicit;
- a leading-order population boundary $\lambda_c^{\text{pop}} \propto (\log N/N)^{1/4}$;
- independent symbolic, numerical, and operational validation of these statements.

What is not claimed is:

- a universal theorem for arbitrary nonlinear or non-Gaussian hidden-variable architectures;
- a proof of the first nonzero post-quartic term exactly at strict coalescence;
- a minimax impossibility theorem for all possible tests;
- a fully explicit bridge to every application-specific parametrization.

Appendix B: Exact Spectrum and Relative Perturbation

The model in Eq. (1) can be written with the lag operator L as

$$(1 - aL)X_t = \lambda F_{t-1} + \epsilon_t, \quad (1 - bL)F_t = \eta_t. \quad (\text{S1})$$

In frequency space,

$$X(\omega) = \frac{\epsilon(\omega)}{1 - ae^{-i\omega}} + \lambda \frac{e^{-i\omega}\eta(\omega)}{(1 - ae^{-i\omega})(1 - be^{-i\omega})}. \quad (\text{S2})$$

Because ϵ and η are independent and white, the observed spectrum is

$$\begin{aligned} S_{\text{true}}(\omega; \lambda) &= \frac{\sigma_\epsilon^2}{|1 - ae^{-i\omega}|^2} + \frac{\lambda^2 \sigma_\eta^2}{|1 - ae^{-i\omega}|^2 |1 - be^{-i\omega}|^2} \\ &= \frac{\sigma_\epsilon^2}{P_a(\omega)} + \frac{\lambda^2 \sigma_\eta^2}{P_a(\omega) P_b(\omega)}. \end{aligned} \quad (\text{S3})$$

Writing $S_0(\omega) = \sigma_\epsilon^2/P_a(\omega)$ gives the relative perturbation form

$$S_{\text{true}}(\omega; \lambda) = S_0(\omega)(1 + \lambda^2 h(\omega)), \quad h(\omega) = \frac{\sigma_\eta^2}{\sigma_\epsilon^2} \frac{1}{P_b(\omega)}. \quad (\text{S4})$$

Appendix C: Local Whittle Geometry of the One-Pole Manifold

Relative Coordinates Near the Null Point

Let

$$\tilde{a} = a + \delta a, \quad \tilde{\sigma}^2 = \sigma_\epsilon^2 + \delta\sigma^2. \quad (\text{S5})$$

Then

$$\frac{S_{\text{null}}(\omega; \tilde{a}, \tilde{\sigma}^2)}{S_0(\omega)} = \left(1 + \frac{\delta\sigma^2}{\sigma_\epsilon^2}\right) \frac{P_a(\omega)}{P_{a+\delta a}(\omega)} = 1 + u\tilde{e}_1 + v\tilde{e}_2 + O(u^2 + v^2 + uv), \quad (\text{S6})$$

with

$$u = \frac{\delta\sigma^2}{\sigma_\epsilon^2}, \quad v = \delta a, \quad \tilde{e}_1(\omega) = 1, \quad \tilde{e}_2(\omega) = \frac{2(\cos\omega - a)}{P_a(\omega)}. \quad (\text{S7})$$

The tangent space is therefore $\mathcal{T} = \text{span}\{\tilde{e}_1, \tilde{e}_2\}$.

Population Whittle Geometry

For two spectra S_1, S_2 , the normalized population Whittle/Kullback-Leibler divergence is

$$D_{\text{KL}}(S_1 \| S_2) = \frac{1}{4\pi} \int_{-\pi}^{\pi} \left[\frac{S_1(\omega)}{S_2(\omega)} - \log \frac{S_1(\omega)}{S_2(\omega)} - 1 \right] d\omega. \quad (\text{S8})$$

Using the scalar expansion $(1 + \delta) - \log(1 + \delta) - 1 = \delta^2/2 + O(\delta^3)$ gives the local quadratic reduction

$$D_{\text{KL}}(S_{\text{true}}(\cdot; \lambda) \| S_{\text{null}}(\cdot; \tilde{a}, \tilde{\sigma}^2)) = \frac{1}{4} \|\lambda^2 h - u\tilde{e}_1 - v\tilde{e}_2\|_{L^2}^2 + O((|u| + |v| + \lambda^2)^3). \quad (\text{S9})$$

Orthogonality of the tangent basis

The orthogonality is exact, not heuristic. Jensen's formula gives

$$\frac{1}{2\pi} \int_{-\pi}^{\pi} \log P_a(\omega) d\omega = 0 \quad (|a| < 1), \quad (\text{S10})$$

and differentiation with respect to a yields

$$0 = \frac{1}{2\pi} \int_{-\pi}^{\pi} \frac{2(a - \cos\omega)}{P_a(\omega)} d\omega = -\langle \tilde{e}_1, \tilde{e}_2 \rangle. \quad (\text{S11})$$

Differentiating once more gives

$$\partial_a \tilde{e}_2 = -\frac{2}{P_a} + \frac{4(\cos\omega - a)^2}{P_a^2} = -\frac{2}{P_a} + \tilde{e}_2^2, \quad (\text{S12})$$

from which the norm of \tilde{e}_2 follows. The tangent basis is therefore orthogonal:

$$\langle \tilde{e}_1, \tilde{e}_2 \rangle = 0, \quad \|\tilde{e}_1\|^2 = 1, \quad \|\tilde{e}_2\|^2 = \frac{2}{1 - a^2}, \quad (\text{S13})$$

so the Gram determinant is positive and the local minimizer is unique.

Appendix D: Projection Coefficients and Pseudo-True Shifts

Basic integrals

For $|c| < 1$,

$$\left\langle 1, \frac{1}{P_c} \right\rangle = \frac{1}{1-c^2}, \quad \left\langle \frac{1}{P_c}, \frac{1}{P_c} \right\rangle = \frac{1+c^2}{(1-c^2)^3}. \quad (\text{S14})$$

Therefore

$$\|h\|^2 = \frac{\sigma_\eta^4}{\sigma_\epsilon^4} \frac{1+b^2}{(1-b^2)^3}. \quad (\text{S15})$$

Projection coefficients

The basic projection integrals are

$$\langle h, \tilde{e}_1 \rangle = \frac{\sigma_\eta^2}{\sigma_\epsilon^2} \frac{1}{1-b^2}, \quad \langle h, \tilde{e}_2 \rangle = \frac{\sigma_\eta^2}{\sigma_\epsilon^2} \frac{2b}{(1-ab)(1-b^2)}. \quad (\text{S16})$$

The second coefficient comes from a contour integral on the unit circle whose poles lie at $z = a$ and $z = b$. The exact residue sum collapses to the rational form in Eq. (S16).

Local pseudo-true shifts

They imply the local pseudo-true shifts

$$\tilde{\sigma}^{2*}(\lambda) = \sigma_\epsilon^2 + \lambda^2 \frac{\sigma_\eta^2}{1-b^2} + O(\lambda^4), \quad (\text{S17})$$

and

$$\tilde{a}^*(\lambda) = a + \lambda^2 \frac{\sigma_\eta^2}{\sigma_\epsilon^2} \frac{b(1-a^2)}{(1-ab)(1-b^2)} + O(\lambda^4). \quad (\text{S18})$$

These shifts are auxiliary to the main theorem but provide a direct check that the best null model moves along the one-pole manifold exactly as predicted by the projection geometry.

Appendix E: Proof of the Quartic Detectability Theorem

Statement Proved Here

In this appendix we prove Theorem 1. Equivalently, for $|a| < 1$ and $|b| < 1$, there exists $\lambda_0(a, b) > 0$ such that for $|\lambda| < \lambda_0(a, b)$ the local minimizer branch exists uniquely and

$$D_{\text{KL,loc}}^{\min}(\lambda) = C(a, b, \sigma_\epsilon, \sigma_\eta) \lambda^4 + O(\lambda^6), \quad (\text{S19})$$

with

$$C(a, b, \sigma_\epsilon, \sigma_\eta) = \frac{\sigma_\eta^4}{2\sigma_\epsilon^4} \frac{b^2(a-b)^2}{(1-b^2)^3(1-ab)^2}. \quad (\text{S20})$$

Remark 1. *The theorem is pointwise in parameter space. Near coalescence, what degenerates is the quartic coefficient C , not the existence of the local expansion itself. The theorem controls the nearby pseudo-true branch, not the global infimum over the full stationary one-pole family.*

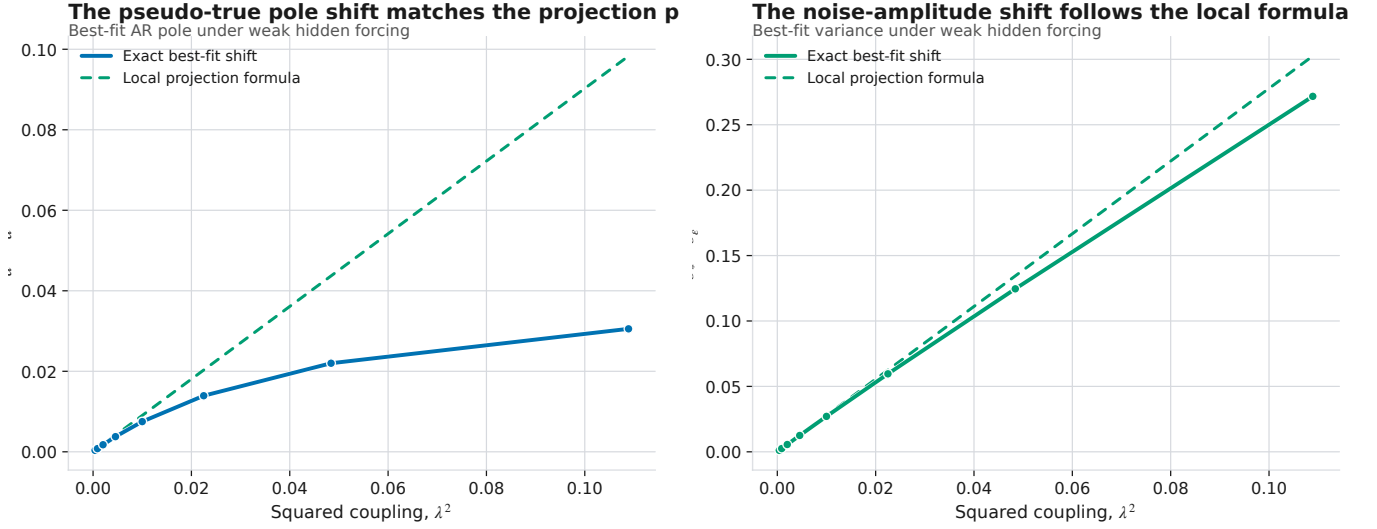


FIG. S1. Auxiliary pseudo-true checks. Left: the leading-order prediction for the best-fit AR pole shift. Right: the corresponding prediction for the best-fit innovation variance shift. Both formulas track the numerical pseudo-true motion of the null model, supporting the projection picture without being part of the principal PRL claim.

Existence and uniqueness of the local branch

The local quadratic reduction in Eq. (S9), together with the positive Gram determinant from Eq. (S13), implies that the Hessian of the reduced objective is strictly positive definite at the null point. The implicit-function theorem therefore gives a unique local minimizer branch $(\tilde{a}^*(\lambda), \tilde{\sigma}^{2*}(\lambda))$ for sufficiently small $|\lambda|$.

Projection formula and residual norm

Let

$$R = h - \Pi_{\mathcal{T}} h. \quad (\text{S21})$$

Because the tangent directions are orthogonal, the residual norm is

$$\|R\|^2 = \|h\|^2 - \frac{\langle h, \tilde{e}_1 \rangle^2}{\|\tilde{e}_1\|^2} - \frac{\langle h, \tilde{e}_2 \rangle^2}{\|\tilde{e}_2\|^2}. \quad (\text{S22})$$

Substituting the exact projection integrals yields

$$\|R\|^2 = \frac{\sigma_n^4}{\sigma_\epsilon^4} \frac{2b^2(a-b)^2}{(1-b^2)^3(1-ab)^2}. \quad (\text{S23})$$

Together with Eq. (11), this proves Eq. (S19). Positivity is immediate because every factor in Eq. (S20) is nonnegative on $|a| < 1$, $|b| < 1$, and the only zeros are $b = 0$ or $a = b$.

What This Appendix Does and Does Not Prove

The theorem above identifies the nearby pseudo-true branch and the asymptotic law for its local minimum. It does not prove that the same expansion controls the global infimum over the full stationary one-pole class. That stronger statement is instead checked numerically in Appendix I by exact global population minimization over the full parameter domain.

Appendix F: Corollaries and the Local Tangent-Absorption Criterion

Coalescence law

The quartic coefficient factorizes as

$$C(a, b, \sigma_\epsilon, \sigma_\eta) = \frac{\sigma_\eta^4}{2\sigma_\epsilon^4} \frac{b^2}{(1-b^2)^3(1-ab)^2} (a-b)^2, \quad (\text{S24})$$

so

$$C \propto (a-b)^2 \quad \text{as } b \rightarrow a. \quad (\text{S25})$$

Population boundary

The corresponding leading-order population boundary is

$$\lambda_c^{\text{pop}}(N) = \left[\frac{\Delta k \sigma_\epsilon^4 (1-b^2)^3 (1-ab)^2 \log N}{\sigma_\eta^4 b^2 (a-b)^2} \frac{1}{N} \right]^{1/4} (1 + o(1)), \quad (\text{S26})$$

which reduces to Eq. (19) for the effective two-pole alternative with $\Delta k = 2$.

Abstract geometric criterion

The solvable model above isolates a broader local criterion. Let \mathcal{M} be a smooth spectral manifold through S_0 . If the leading perturbation enters as

$$S_{\text{true}}(\lambda) = S_0(1 + \lambda^2 h + O(\lambda^4)), \quad (\text{S27})$$

and if the local Whittle Hessian on the tangent space \mathcal{T} of \mathcal{M} is positive definite, then the same quadratic reduction gives a unique local minimizer branch and

$$D_{\text{KL,loc}}^{\min}(\lambda) = \frac{\lambda^4}{4} \|(I - \Pi_{\mathcal{T}})h\|^2 + O(\lambda^6). \quad (\text{S28})$$

This statement is intended as a geometric criterion, not as a stand-alone theorem for arbitrary model classes: making it theorem-grade would require explicit assumptions on parameterization, norms, and remainder control beyond what is needed for the solvable one-pole case.

What Is Not Proved Here

The theorem package establishes the quartic law and its exact prefactor within the one-pole projection class. It does not prove the first nonzero post-quartic coefficient at strict coalescence, and it does not claim a universal law for arbitrary hidden-variable architectures.

Appendix G: Enriched Null Families and the ARMA(1,1) Corollary

ARMA(1,1) one-pole null family

The simplest enriched null class keeps a single relaxation pole but adds one moving-average zero:

$$S_{\text{null}}^{(1,1)}(\omega; \tilde{a}, \theta, \tilde{\sigma}^2) = \tilde{\sigma}^2 \frac{P_\theta(\omega)}{P_{\tilde{a}}(\omega)}. \quad (\text{S29})$$

At the AR(1) null point $(\tilde{a}, \theta, \tilde{\sigma}^2) = (a, 0, \sigma_\epsilon^2)$, the relative expansion becomes

$$\frac{S_{\text{null}}^{(1,1)}(\omega; \tilde{a}, \theta, \tilde{\sigma}^2)}{S_0(\omega)} = 1 + u\tilde{e}_1 + v\tilde{e}_2 + w\tilde{e}_3 + O(u^2 + v^2 + w^2 + uv + uw + vw), \quad (\text{S30})$$

with

$$w = \theta, \quad \tilde{e}_3(\omega) = -2 \cos \omega, \quad (\text{S31})$$

and the previously defined \tilde{e}_1, \tilde{e}_2 . Thus the tangent space is enlarged to

$$\mathcal{T}_{(1,1)} = \text{span}\{\tilde{e}_1, \tilde{e}_2, \tilde{e}_3\}. \quad (\text{S32})$$

Gram matrix and projection data

The extra tangent direction has the exact inner products

$$\langle \tilde{e}_1, \tilde{e}_3 \rangle = 0, \quad \langle \tilde{e}_2, \tilde{e}_3 \rangle = -2, \quad \|\tilde{e}_3\|^2 = 2. \quad (\text{S33})$$

Hence, for generic $a \neq 0$, the three-dimensional Gram matrix is

$$G_{(1,1)} = \begin{pmatrix} 1 & 0 & 0 \\ 0 & 2 & -2 \\ 0 & 1 - a^2 & 2 \end{pmatrix}, \quad \det G_{(1,1)} = \frac{4a^2}{1 - a^2} > 0. \quad (\text{S34})$$

The nongeneric point $a = 0$ is degenerate because \tilde{e}_2 and \tilde{e}_3 are collinear there ($\tilde{e}_2 = -\tilde{e}_3$).

The new projection coefficient is also explicit:

$$\langle h, \tilde{e}_3 \rangle = -\frac{2b\sigma_\eta^2}{\sigma_\epsilon^2(1 - b^2)}. \quad (\text{S35})$$

Together with Eq. (S16), this closes the three-dimensional projection problem completely.

Closed quartic coefficient

Proposition 1. *For generic $a \neq 0$ with $|a| < 1$ and $|b| < 1$, local Whittle minimization over the ARMA(1, 1) one-pole null family gives*

$$D_{\text{KL,loc,(1,1)}}^{\min}(\lambda) = C_{(1,1)}(a, b, \sigma_\epsilon, \sigma_\eta)\lambda^4 + O(\lambda^6), \quad (\text{S36})$$

with the exact coefficient

$$C_{(1,1)} = \frac{\sigma_\eta^4}{2\sigma_\epsilon^4} \frac{b^4(a - b)^2}{(1 - b^2)^3(1 - ab)^2} = b^2 C. \quad (\text{S37})$$

The proof is the same projection argument as in Appendix E, but now with $\Pi_{\mathcal{T}_{(1,1)}}$ in place of $\Pi_{\mathcal{T}}$. Since the enlarged tangent space absorbs one extra component of h , the quartic coefficient is reduced by a factor of b^2 relative to the strict AR(1) null, but the coalescence factor $(a - b)^2$ and the quartic onset in λ survive unchanged. Direct numerical evaluation of the three-dimensional projection reproduces Eq. (S37) to machine precision for representative parameter sets, and Appendix J reports an operational Whittle-BIC stress test with this enriched null.

Appendix H: Independent Symbolic Verification

Symbolic identities checked exactly

A separate symbolic pipeline verifies, without numerical substitution:

1. the contour-integral identity that gives Eq. (S16);
2. the exact residual norm in Eq. (S23);
3. the factorization of the coalescence term $(a - b)^2$;
4. the positivity of the Gram determinant from Eq. (S13).

These checks close the main algebraic loophole in the theorem package: the quartic coefficient does not rely on a single hand derivation.

Why this matters

The symbolic layer makes the theorem harder to attack. The coefficient no longer rests on a single contour-integral route; it is fixed both by direct analysis and by an independent algebraic verification chain.

Appendix I: Exact Numerical KL Validation

Baseline parameter set

Unless otherwise stated, the numerical tests use the baseline parameters

$$(a, b, \sigma_\epsilon^2, \sigma_\eta^2) = (0.95, 0.8, 1, 1). \quad (\text{S38})$$

The exact-population validation never inserts the local asymptotic formula into the objective. Instead, for each coupling value we minimize the full Whittle/KL divergence over the stationary one-pole parameter domain and then compare the resulting minimum to the theorem-level prediction.

Quartic and threshold laws

Exact population minimization of the Whittle objective over the one-pole class gives a quartic slope of 2.67918 for $\lambda \leq 0.15$. For the baseline parameters in Eq. (S38), the quartic approximation remains accurate to within about 10% for $\lambda \lesssim 0.15$. Solving $ND_{\text{KL}}^{\text{min,num}}(\lambda_c) = \log N$ over $N \in \{200, 400, 800, 1600, 3200, 6400, 12800\}$ gives a threshold slope of -0.254360 .

Coalescence law

Extracting the quartic coefficient on the window $\lambda \in \{0.005, 0.0075, 0.01, 0.015\}$ and sweeping b toward a gives a normalized coalescence slope of 1.922526. At strict coalescence, $D_{\text{KL}}^{\text{min,num}}/\lambda^4$ keeps decreasing as $\lambda \rightarrow 0$, confirming that the quartic coefficient truly vanishes.

Pseudo-true shifts

The same exact numerical optimization returns the best-fit one-pole parameters. Their motion agrees with Eqs. (S17) and (S18), providing an additional numerical check of the projection geometry.

Appendix J: Operational Monte Carlo Validation

Model-selection rule

The operational model-selection benchmark compares the one-pole null against the effective two-pole alternative

$$S_{\text{alt}}(\omega) = \frac{\sigma^2}{P_a(\omega)} + \frac{q}{P_a(\omega)P_b(\omega)}, \quad (\text{S39})$$

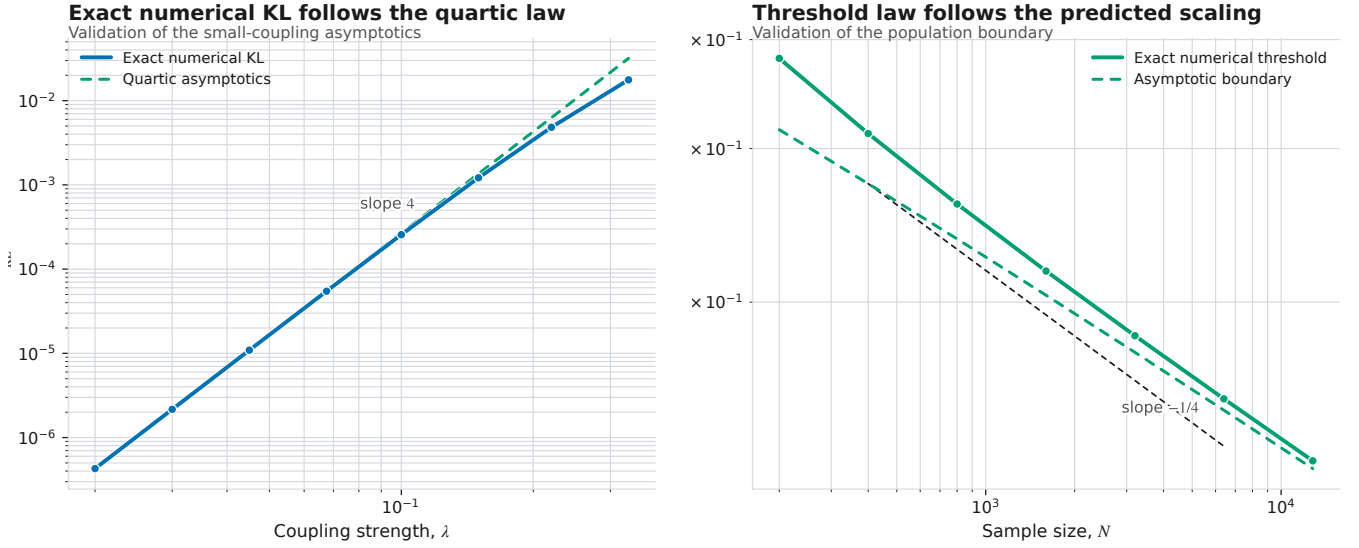


FIG. S2. Supplementary numerical validation. Left: exact numerical Whittle minimization confirms the quartic coupling law. Right: the same population solver confirms the threshold scaling predicted by the closed-form coefficient.

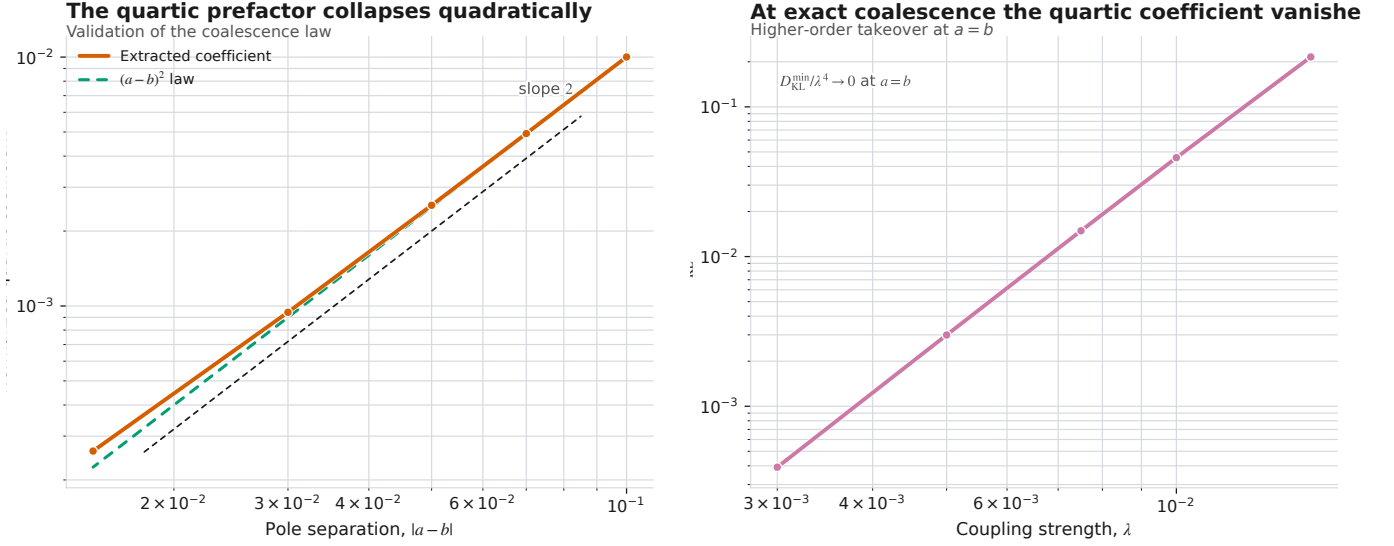


FIG. S3. Coalescence validation. Left: the extracted quartic coefficient collapses as $(a - b)^2$. Right: at strict coalescence, $D_{\text{KL},\text{loc}}^{\min}(\lambda)/\lambda^4$ keeps decreasing as $\lambda \rightarrow 0$, confirming that the quartic coefficient vanishes.

with $\Delta k = 2$. We fit both models by the Whittle likelihood and declare the hidden driver detected when $\text{BIC}_{\text{alt}} < \text{BIC}_{\text{null}}$. Only the observed series $\{X_t\}_{t=1}^N$ is retained in each synthetic trial. This benchmark is intentionally favorable in one respect: the alternative contains the exact observed spectrum family generated by Eq. (1). Its role is therefore not to prove robustness to arbitrary model uncertainty, but to ask whether the theorem-scale boundary is already visible when the alternative structure is known. All reported intervals are Wilson 95% intervals for binomial detection frequencies.

Collapse experiment

For the strengthened experiment, we use 200 repetitions per grid point, sample sizes $N = 256, 512, 1024, 2048$, and scaled couplings $\lambda/\lambda_c^{\text{pop}}(N) \in \{0.6, 0.8, 1.0, 1.2, 1.5\}$. At the predicted boundary, the detection probabilities are

0.385, 0.410, 0.535, and 0.505. The corresponding 95% Wilson intervals are approximately [0.320, 0.454], [0.344, 0.479], [0.466, 0.603], and [0.436, 0.574]. The mean spread across N at fixed scaled coupling is 0.138, and the mean Wilson width at the predicted boundary is about 0.136. The interpolated 50%-power points are $r_{50}(N) = 1.100, 1.053, 0.982,$ and 0.997.

Role in the PRL package

This experiment is the bridge from theorem to operational relevance. The strongest defensible claim is not exact finite-size collapse, but a common turnover near the predicted scaled boundary together with convergence of the effective crossover toward unity.

Hard synthetic stress tests

Null calibration remains stringent: under $\lambda = 0$, the false-positive rate stays at or below 0.5% for $N = 256$ through 2048, with Wilson upper bounds below 0.026 and mean ΔBIC values between about -8.8 and -13.3 in favor of the null. The same scaled-turnover picture also persists across well-separated, moderate, and near-coalescent parameter regimes, as shown in Fig. S4. For these three regimes, the detection power at $\lambda/\lambda_c^{\text{pop}} = 1.0$ spans the range 0.400 to 0.656, while at $\lambda/\lambda_c^{\text{pop}} = 1.15$ it spans 0.633 to 0.878. Near coalescence, the mean ΔBIC is slightly negative at the nominal boundary for smaller N , but becomes strongly positive above it, exactly as the asymptotic interpretation predicts.

Mild innovation misspecification

The operational boundary is not restricted to exact Gaussian innovations. Keeping the same linear dynamics but replacing both innovations by standardized Student- t_5 noise leaves the boundary-region picture intact. For the baseline parameters, the Whittle-BIC detection powers are 0.433 and 0.544 at $\lambda/\lambda_c^{\text{pop}} = 1.0$ for $N = 512$ and 2048, with corresponding Wilson intervals [0.336, 0.536] and [0.442, 0.643]. At $\lambda/\lambda_c^{\text{pop}} = 1.25$, the powers rise to 0.833 and 0.922, with Wilson intervals [0.743, 0.896] and [0.848, 0.962]. This test does not preserve every exact theorem-level coefficient, but it does show that turnover near the predicted scaled boundary survives a mild distributional mismatch between generator and fitted model.

Enriched-null operational stress test

A more demanding null replaces the strict AR(1) fit by the enriched one-pole ARMA(1, 1) family from Appendix G. The null then has one extra parameter, so the model-count gap drops to $\Delta k = 1$ and the relevant scaled coupling is the corresponding local boundary $\lambda_{c,(1,1)}^{\text{pop}}$. For the baseline parameters and 80 repetitions per grid point, the detection powers at $\lambda/\lambda_{c,(1,1)}^{\text{pop}} = \{0.8, 1.0, 1.15\}$ are (0.188, 0.412, 0.650) for $N = 512$ and (0.250, 0.563, 0.775) for $N = 2048$. The interpolated 50%-power locations are $r_{50}(512) \approx 1.06$ and $r_{50}(2048) \approx 0.97$. Thus the enriched null weakens detectability substantially, exactly as the analytic coefficient $C_{(1,1)} = b^2 C$ predicts, but it does not destroy the boundary-centered turnover. The runs are generated by the dedicated ARMA-null stress script and summarized alongside the main stress suite in the repository results.

Appendix K: Continuous-Time Foundation and Scope

Continuous-time driven OU foundation

The discrete-time theorem was motivated by the continuous-time driven Ornstein-Uhlenbeck system

$$\dot{X} = -\gamma X + \lambda F + \sqrt{2D} \xi_X(t), \quad \dot{F} = -\alpha F + \sqrt{2D_F} \xi_F(t). \quad (\text{S40})$$

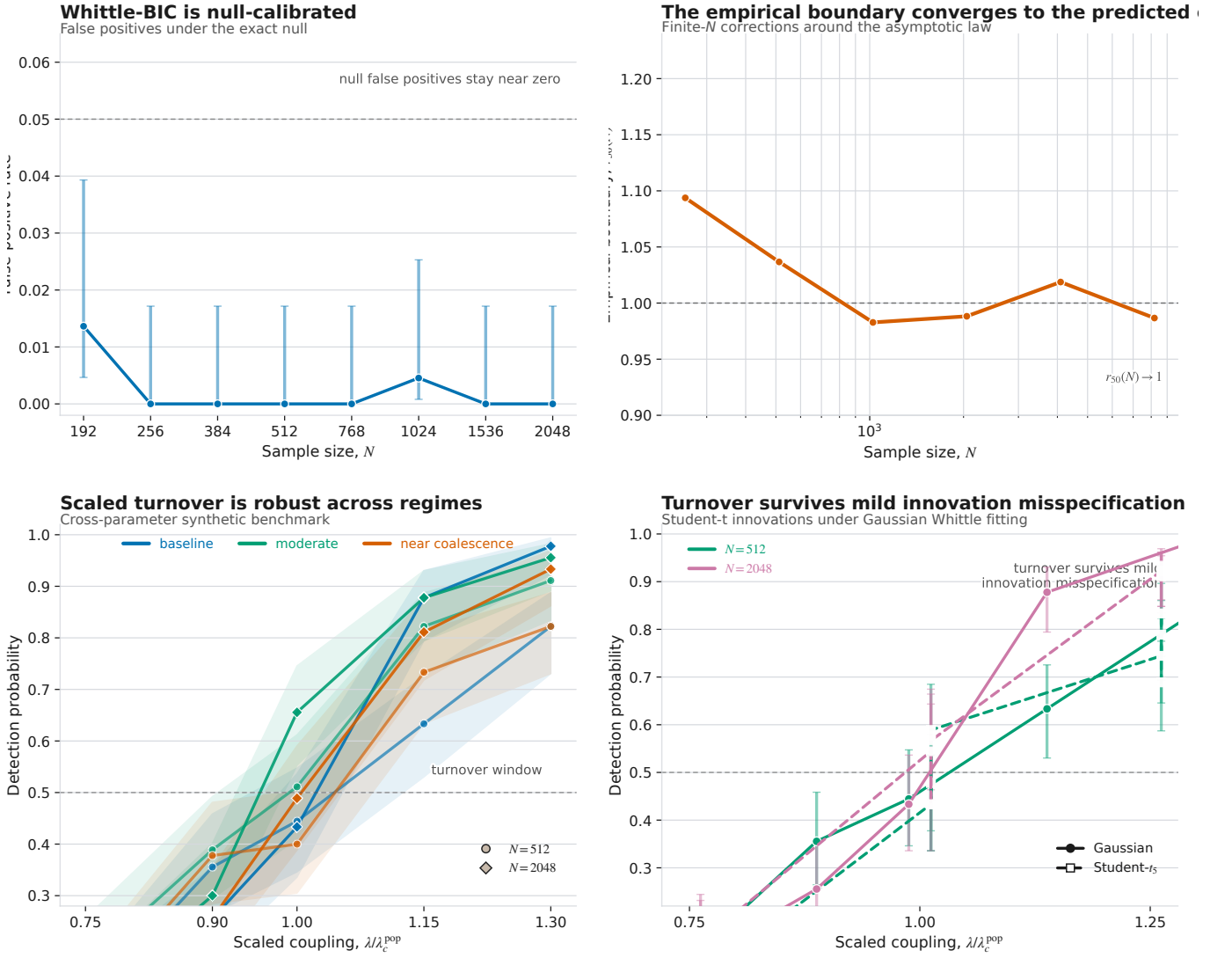


FIG. S4. Hard synthetic stress tests. Top left: the operational Whittle-BIC procedure is null-calibrated. Top right: the empirical boundary converges toward the predicted scaled boundary. Bottom left: the turnover picture persists across distinct (a, b) regimes. Bottom right: it survives mild innovation misspecification.

Its exact observed spectrum is

$$S_X(\omega) = \frac{2D}{\gamma^2 + \omega^2} + \frac{2D_F\lambda^2}{(\gamma^2 + \omega^2)(\alpha^2 + \omega^2)}. \quad (\text{S41})$$

When $\alpha = \gamma$, the leading perturbation is proportional to $(\gamma^2 + \omega^2)^{-2}$ and becomes tangent to the one-pole OU manifold. This is the continuous-time precursor of the discrete-time coalescence law.

Why the theorem is completed in discrete time

The continuous-time picture is structurally correct but less convenient for a complete theorem because the frequency domain is unbounded and the weighted absolute-space formulation requires additional care at high frequency. In discrete time, the frequency interval is compact and the projection algebra closes cleanly in standard L^2 .

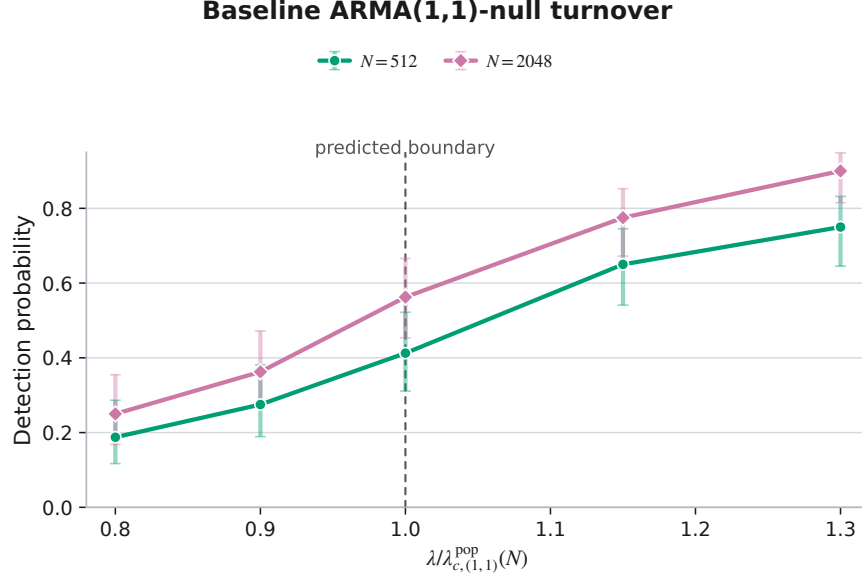


FIG. S5. Baseline enriched-null operational turnover. For the baseline parameters in Eq. (S38), the strict AR(1) null is replaced by the one-pole ARMA(1, 1) family, and detection probability is plotted against the corresponding local boundary $\lambda_{c,(1,1)}^{\text{pop}}(N)$ for $N = 512$ and 2048 . The turnover persists, but the enriched null shifts the crossover upward at smaller N , consistent with the reduced quartic coefficient $C_{(1,1)} = b^2 C$.

Back-of-the-envelope physical scale estimates

The climate-style relevance statement in the main text can be quantified directly from Eq. (S26). For equal noise scales and $(a, b) = (0.90, 0.80)$, the population boundary is

$$\lambda_c^{\text{pop}}(10^3) \approx 0.30, \quad \lambda_c^{\text{pop}}(10^4) \approx 0.18. \quad (\text{S42})$$

For the near-coalescent choice $(a, b) = (0.90, 0.88)$, the same formula gives

$$\lambda_c^{\text{pop}}(10^3) \approx 0.39, \quad \lambda_c^{\text{pop}}(10^4) \approx 0.23. \quad (\text{S43})$$

The colloidal-probe estimate quoted in the main text uses this same near-coalescent boundary law as an illustrative physical reading of Eq. (S26), rather than as an independent application-specific calculation. Thus modest pole coalescence already raises the leading-order threshold by a visible amount. More generally, at fixed scaled coupling $\lambda/\lambda_c^{\text{pop}}$,

$$\frac{N}{\log N} \propto |a - b|^{-2}, \quad (\text{S44})$$

so shrinking the pole separation from 0.10 to 0.02 raises the leading-order data requirement by roughly a factor of 25. These are not application-specific claims; they are order-of-magnitude consequences of the exact solvable boundary law.

Scope and non-claims

The present theorem package proves:

- an exact quartic detectability law in the one-pole projection class;
- an exact closed form for the quartic coefficient;
- a quantitative coalescence law $C \propto (a - b)^2$;

- a leading-order population boundary $\lambda_c^{\text{pop}} \propto (\log N/N)^{1/4}$;
- symbolic, numerical, and operational support for these statements.

It does not claim a universal theorem for arbitrary hidden-variable architectures, nor the first nonzero post-quartic coefficient exactly at strict coalescence. For richer null families, one expects a larger tangent space, a smaller leading normal component, and therefore a weaker detectability coefficient; if the null family can already represent the driver-induced multipole structure, the first nonzero detectability term may occur at still higher order.